Patch-like, two dimensional WSe2-based hetero-structures activated by a healing catalyst for H2 photocatalytic generation

Pierre-Louis Taberna, Juliana Barros Barbosa, Andrea Balocchi, Iann C Gerber, Koki Urita, Antoine Barnabé, Xavier Marie, Jean Yves Chane-ching

Patch-like, Two Dimensional WSe_2-Based Hetero-structures Activated by a Healing Catalyst for H_2 Photocatalytic Generation.

P. L. Taberna[†], J. Barros Barbosa[†], A. Balocchi[ŧ], I. Gerber[ŧ], K. Urita[₮], A. Barnabe[†], X. Marie[ŧ], J. Y. Chane –Ching[†]*

[†]Université de Toulouse, UPS, CNRS, CIRIMAT, 118 Route de Narbonne, F-31062, Toulouse, France

[ŧ]Université de Toulouse, INSA-CNRS-UPS, LPCNO, 135 Av. Rangueil, 31077 Toulouse, France

[₮] Department of Engineering, Nagasaki University, 1-14 Bunkyo-machi, Nagasaki, 852-8521, Japan.

Abstract

2D photoactive materials may offer interesting opportunities in photocatalytic devices since they combine strong light absorption and shortening of charge carrier's diffusion path. Because of their high surface defect concentration and the formation of a majority of edge/plane vs plane/plane contacts between the anisotropic building blocks, surface defect passivation and improvement of charge carrier transport are critical for the large development of high surface area, 2D photo-catalysts. Here, we propose a hetero-structure nanoporous network with a patch-like coating as high performance 2D photo-catalysts. The hetero-structured building blocks are composed of a photo-active WSe_2 nanoflake in direct contact both with a conducting rGO nanosheet and with an ultrathin layer of healing catalyst. The resulting nanoporous film achieves a photocurrent density for H_2 evolution up to 5 mA cm^{-2} demonstrating that the patch-like hetero-structures have been used as an effective strategy to improve at once hole collection, defect passivation and charge transfer. These hetero-structures made of an ultrathin layer of healing catalyst represent promising building blocks for the bottom-up fabrication of high surface area photocathodes particularly suited for 2D photo-catalysts displaying high defect concentration.

Keywords: Hydrogen evolution reaction; Photocatalysts; 2D materials; Water splitting; Mo sulfide catalysts.

1. Introduction

Hydrogen production from photocatalytic solar water splitting represents a critical step for clean, efficient renewable and sustainable energy conversion [1,2]. Intense researches on various synthetic processes including Physical Vapor Deposition [3], Chemical Vapor Deposition [4], soft chemistry [5], or self-assembly of nano-sized building blocks [6] were devoted to the design and fabrication of efficient nanostructured photo-electrodes in order to greatly increase their performances. Champion photo electrode nanostructures [4-5] for solar water splitting generally exhibit high surface area, defect-free, highly crystallized photoactive materials which are usually achieved at high temperatures, T > 450 °C. Designing innovative and more efficient photo-catalyst nanostructures remains a prerequisite for the large scale development of solar photocatalytic water splitting. Various strategies have been proposed for film nano-structure optimization including formation of intimate nanojunctions between a photoactive material and a catalyst [7], nanopore size control [5], or achievement of a low proportion of high-angle grain boundaries between primary crystallites forming the photoactive film [4]. Recently, new opportunities have emerged with the discovery of the vast library of 2D materials displaying unique optoelectronic properties [8-10]. Indeed, the high anisotropic form factor displayed by these 2D materials favors maximum sunlight harvesting and promotes the mass transfer of reactants and products. More important, these 2D materials may drastically shorten diffusion length of photo-generated charge carriers thus minimizing their recombination. Interestingly, these 2D materials can develop increased contact areas between the photoactive nanosheets and planar co-catalysts which are beneficial for the separation of electrons/holes diminishing the barrier for electron transport through the co-catalyst. Thus, particular attention has been paid to the formation and role of 2D/2D interfaces. Recent construction strategies for the photocatalytic decomposition of pollutants or for the hydrogen evolution reaction proposed 2D/2D heterojunctions [11-15] including p/n hetero-junctions [11] or co-catalyst/photoactive nanosheets hetero-structures [11]. Among these 2D materials, 2D Transition Metal Di Chalcogenides (TMDC) nanosheets and nanoflakes are interesting photoactive materials [9] displaying unique light absorption properties [16] combined with appropriate band conduction levels for the Hydrogen Evolution Reaction (HER) [17-18]. More particularly,

TMDC materials are ideal candidates for tandem cells fabrication because they display various HER onset potentials and adjustable band gaps depending of their chemical composition [19-20] and thickness, i.e. varying from monolayer to a few layers [9]. Despite the recent development of 2D photocatalysts, they still face several significant challenges: (1) The high concentration of surface defects of these 2D materials [21] acting as recombination sites for the charge carriers, has greatly hampered the development of these materials in photo-catalysis. Various strategies have been already proposed to passivate these defects [6, 22-23], improving their performances in water splitting. Particularly, the design of a multicomponent film achieving defects passivation and possessing catalytic properties [6, 24] should offer the advantage of a better control of the film microstructure. (2) Another important obstacle hindering their development in practical applications is their low surface area [8]. Although recent efforts have focused on the design of macroporous architectures [25], their nanoporous counterparts constructed from these 2D materials yielding higher surface areas generally suffer from poor charge carrier transport due to a majority of edge/edge or edge/plane vs plane/plane contacts. Thus, it is highly desirable to develop innovative routes for the design of new nanostructured films fabricated from 2D photo-catalysts and displaying high photo-electrochemical performances.

In this work, a nanoporous network of patch-like hetero-structures fabricated from 2D WSe_2 nanoflakes and including an ultrathin layer of healing co-catalyst is proposed for the photocatalytic water splitting. 2D WSe_2 was chosen as 2D materials because of its band gap properties (1.5 eV) which closely match the solar spectrum [9] and its high stability in acidic or alkaline solutions. The hetero-structured nanoporous network have been first designed to improve the photo-generated hole collection through the implementation of a percolating network of conducting reduced Graphene Oxide (rGO) nanosheets connected to the Fluorine-doped Tin Oxide (FTO) back electrode. Taking advantage of their analogous layered structures, we have thus focused in a first step on the construction of WSe_2/rGO layered heterojunctions with partial coverage of the WSe_2 surface by the rGO nanosheets. The patch-like, high surface area, layered hetero-structure was prepared in this first step by a co-self-assembly process of WSe_2 nanoflakes and Graphene Oxide (GO) nanosheets of lower lateral size. GO nanosheets which were later transformed into rGO by thermal reduction under Ar atmosphere, were chosen because they interact with the WSe_2 nanoflakes by amphiphilic interactions [26]. Indeed, GO nanosheet acts as an amphiphilic surfactant, in

binding to WSe_2 through the hydrophobic, un-oxidized, poly-aromatic islands located in its basal plane while the hydrophilic (i.e. carboxyl and hydroxyl) groups on the edges ensure the colloidal stabilisation of the GO/WSe_2 ensemble in dimethylformamide (DMF). In addition to this amphiphilic ~~hydrophilic~~ interaction, the formation of the WSe_2 nanoporous layered hetero-structure was driven by short-range complexing interactions between the WSe_2 surface and a sacrificial template. For this purpose, a customized nanometer-size, colloidal, mixed-metallic sulfide ($Sn_{0.5}Sb_{0.5}S_{1.5}$) template interacting with the TMDC nanoflakes surface was specially-engineered and synthesized to ensure minimal oxidation of the WSe_2 thin nanoflakes during the whole self-assembly process. In a second step, simultaneous surface defect passivation of the photoactive 2D WSe_2 and its catalytic activation were performed yielding the co-catalyst/ WSe_2/rGO hetero-structure network. To preserve its high surface area, we have used a multicomponent ultrathin film displaying multifunctional properties to homogeneously coat the photoactive film. This film composed of different thio- and oxo-thio-Mo complexes denoted in the following Mo_xS_y, includes thio- and oxo-thio-Mo monomers with healing properties while presence of thio- and oxo-thio-Mo dimers and trimers develop catalytic properties [6]. Using high resolution transmission microscopy (HR-TEM) and Intensity Modulated Photocurrent Spectroscopy (IMPS), we demonstrate the patch-like coating of the WSe_2 photo-active surface respectively by the rGO conductive nanosheets and the healing co-catalyst film. High photocurrents up to 5 mA cm^{-2} under 1 sun illumination were achieved highlighting the beneficial use of a healing co-catalyst in the fabrication of these patch-like hetero-structures.

2. Methods.

2.1. Materials

Preparation of MoxSy/WSe_2/rGO hetero-structures.

Preparation of Sn(IV)-Sb_2S_3 (Sb=0.5 $_{molar}$) colloids. $SbCl_3$ (Sigma, 8 mmol, 1.83 g) and $SnCl_4$ $5H_2O$ (Sigma, 8 mmol, 2.8 g) are dissolved in 32 ml dimethylsulfoxide (DMSO). A $(NH_4)_2S$ aqueous solution is prepared by adding H_2O to 3.23 M S^{2-} solution (Sigma, 64 mmol, 19.81 ml) to a total volume of 128 ml. Precipitation of a brown solid is observed after the instantaneous addition of the DMSO metallic salts solution to the sulfide solution. After stirring one night at room temperature (RT), the reaction mixture is aged at 30 °C (two days)

until a yellow limpid solution containing the anionic metallic chalcogenide species is obtained. After dilution of the freshly prepared anionic chalcogenide solution (20 ml of the mother solution diluted to 200 ml by H_2O), temperature polycondensation of the soluble anionic species is performed in a pre-heated constant temperature bath at 65 °C. When the solution turns to yellow green turbid (2 hours), the reaction is immediately quenched by addition of 200 ml H_2O to the solution. After aging for one night at RT, the colloidal solution is washed on a 3 KD membrane by 200 ml H_2O and finally post-concentrated by ultrafiltration yielding an orange colloidal dispersion. Transfer in (DMF) is performed by adding DMF into the aqueous dispersions and slow evaporation during 16 h in Air atmosphere at 65 °C.

WSe_2/rGO co-textured powder formation. WSe_2 powder (Alfa Aesar) was exfoliated in solvent [27] using an ultrasonicator 750 W at 40% amplitude. The Di Chloro Benzene (DCB) solvent-exfoliated WSe_2 nanoflakes were collected after size-fractionation (selection at 800 rpm) and redispersion in DMF. The WSe_2 (40 g l^{-1}) and $Sn_{0.5}Sb_{0.5}S_{1.5}$ (100 g l^{-1}) DMF concentrated colloidal dispersions were mixed at room temperature at a WSe_2 volume fraction, Φv_{WSe2}, $\Phi v_{WSe2}= V_{WSe2}/(V_{WSe2}+V_{SnSbS})= 0.15$. Then, 1 ml of GO dispersion (1 g l^{-1}, lateral size L= 80 nm) was added to the previous mixture to achieve a r_{rGO} molar ratio, $r_{rGO}= rGO/(rGO+WSe_2)$, rGO= 0.05. The resulting solution was poured in a large surface open reactor and evaporated at room temperature under a hood equipped with Air flow. The resulting dried co-textured powder was collected and calcined under Ar at 200 °C during 1 hour. Dissolution of the template from the co-textured powder was performed by adding 20 ml of $(NH_4)_2S$ 1.5 M. This operation was performed 3 times and the powder was finally washed in H_2O. No trace of Sn or Sb was detected by energy dispersive spectroscopy (EDS) analysis on the WSe_2/rGO dried co-textured powder.

WSe_2/rGO photo-electrodes. The photo-electrodes were made by drop casting a solution containing the WSe_2/rGO co-textured powder previously described (r_{rGO}= 0.05) dispersed in a GO colloidal aqueous solution to achieve a total rGO content, r_{rGO} = 0.15. Two sets of WSe_2/rGO photoelectrodes (S= 1 cm^2), denoted hereafter nanostructured films, were prepared with deposition of 4 or 8 layers, with solvent (H_2O) evaporation between each layer deposition. Typical average thicknesses of the films were e= 2 and 4 µm respectively achieved with mass loading, m= 2 and 4 mg. The WSe_2/rGO electrodes were post-calcined with a heating rate of 25° h^{-1} under Ar at 300 °C during 2h.

MoxSy healing co-catalyst film deposition. A thio-, oxo-thio-Mo complexe solution is prepared as previously described [6] by dissolving 2.5 millimoles of $(NH_4)_2$ MoS_4 (0.65 g), into 8 ml of 0.31 M $(NH_4)_2S$ solution. The solution is adjusted at pH 9 with 4.5 ml of HCl 0.5 M and diluted to 250 ml. Solid precipitate in small quantity is removed by ultracentrifugation at 15 000 rpm during 10 min. The healing catalyst film is deposited by successive dip coatings (2x 16 h) of the WSe_2/rGO–FTO photo-electrode under slow stirring into the thio-, oxo-thio-Mo complexes solution (0.01M Mo) previously prepared.

2.2. General characterization.

Conductivity measurements were performed using a Signatone S 1060R conductimeter equipped with four QUAD PRO electrodes. Measurements were performed on drop-cast and nanostructured WSe_2-based films deposited on Glass substrates with a film thickness of ~ 2 µm and electrodes inter-distance of 1.6 mm.

Continuous wave photoluminescence (PL) has been performed on the non-coated and co-catalyst coated WSe_2 photocathodes by exciting the samples mounted on an AttoCube atto 700 cryostat with a He-Ne laser (excitation 632.8 nm). The laser light has been focused on the sample using a high numerical aperture lens (NA= 0.55) to a ~ 2 µm spot-size with powers ranging from 50 to 500 µW. The PL signal, collected from the sample in backscattering mode, has been dispersed by an imaging monochromator and the spectrum recorded using a liquid nitrogen-cooled silicon charge coupled device (CCD camera).

(TEM) studies were performed using a JEOL JEM-ARM 200F spherical-aberration probe corrected electron microscope equipped with a cold field emission gun operated at 200 kV. The complete equipment includes an ultrafast Ultrascan 2k x 2k camera (Gatan) for TEM, high-angle annular dark field (HAADF) detectors (JEOL) for STEM imaging, a Centurio X-ray detector (JEOL) for ultra-high resolution EDS mappings. Plan view sections were prepared by Focussed Ion Beam (FIB) The sample is thinned by standard tripod polishing until it is a few µm thick. The final sample is thinned using a Gatan PIPS 691 ion beam miller to create an electron transparent sample.

2.3. Hydrogen and photo-electrochemical measurements.

Linear scanning voltammetry (LSV) curves were recorded using a Gamry potentiostat in a three-electrode configuration equipped with a Pt foil and a Ag/AgCl reference electrode. In a typical LSV acquisition, the voltage applied to the working electrode (S= 1 cm^2) was swept

cathodically (10 mV s^{-1}) between +0.4 V and -0.4 V vs NHE in H_2SO_4 0.5 M for the MoxSy /WSe_2/rGO electrode. The light source used in the photoelectrochemical (PEC) measurements was a 100 W Xe lamp including AM 1.5G filter. By adjusting the distance between the sample and the simulator, we finely controlled the irradiance of 1 sun using a pyranometer (PMA 2144 Solar light).

A three electrode closed set-up was used for the hydrogen detection. The real-time analysis of the composition of the gas was performed using a Gas Chromatograph (Shimadzu, GC-2014 AT). The Faradic efficiency of our cell is calculated assuming 100 % efficiency for a Pt calibration cell equipped with Pt foils as both the working electrode and counter electrode.

Incident-photon-to-current-efficiency (IPCE) measurements of the photocathodes were performed illuminating the photocathode using a set of high-power light emitting diodes (H2A1 Series LED) from Roithner Laser Technik.

IMPS measurements were performed in H_2SO_4 0.5 M for bias range of +0.4 to -0.2 V vs NHE and a frequency range of 0.1 Hz to 10 KHz. The modulated illumination was provided by a light emitting diode (Roithner Laser Technik, λ= 760 nm, 0.4 Watt). The AC amplitude was set up to 40 % of the applied DC base intensity.

3. Results-Discussion.

3.1. 2D WSe_2 nanostructured film by co-self-assembly.

Fabrication of the 2D WSe_2 nanostructured photocatalyst involves the colloidal co-self-assembly of GO nanosheets, WSe_2 nanoflakes of optimal thickness and a post leachable template of controlled size (D= 65 nm, Figure 1a). In a first step, we prepare nanoporous co-textured WSe_2/rGO powder by colloidal self-assembly in DMF of GO nanosheets, solvent-exfoliated WSe_2 nanoflakes and spherical ($Sn_{0.5}Sb_{0.5}S_{1.5}$) colloidal templates (Figure 1b,c and Figure S1). Indeed, Sb_2S_3, which forms highly soluble complexes with sulfide anions [28] proves to be a good candidate as a hard template. Sn(IV) cations were incorporated into Sb_2S_3 to significantly improve the colloidal stabilization of the Sb_2S_3 nanoparticles while providing molecular Sn chalcogenides as surface ligands [29,30]. To fully exploit the layered character of the photo-active film, we select ultrathin GO nanosheets of slightly lower lateral size as building blocks to construct the conducting percolating network. GO nanosheets, instead of graphene [31,32], were used to favour amphiphilic interactions with the WSe_2

nanoflakes building blocks [26] during the co self-assembly process. With the objective to conduct the co-self-assembly in a highly repulsive regime, ($Sn_{0.5}Sb_{0.5}S_{1.5}$) colloids and GO nanosheets building blocks were prepared in highly alkaline aqueous solution (Figure S1), thus developing similar negative surface charge. To prevent any phase separation with the WSe_2 nanoflakes, the co-self-assembly process was driven in DMF solvent. After solvent evaporation, thermal consolidation of the WSe_2/rGO network under Ar at 200 °C and post-dissolution of the ($Sn_{0.5}Sb_{0.5}S_{1.5}$) template in S_2^{2-} aqueous solution, a composite textured powder is collected. To get more insight into the interactions driving the co self-assembly process, we first conducted separately self-assembly of WSe_2 nanoflakes and of GO nanosheets with the ($Sn_{0.5}Sb_{0.5}S_{1.5}$) colloids template. BET measurements performed on the corresponding dried textured powders clearly show the presence of significant pore volume exclusively on the textured WSe_2 sample (Figure S2). This demonstrates that the metallic sulfide colloidal template interacts preferentially with the WSe_2 nanoflakes and not with the GO surfaces. In addition, no phase separation of the GO nanosheets was observed during the co-assembly. Thus, our process probably involves a second interaction regime based on ~~hydrophilic~~ amphiphilic interactions between WSe_2 nanoflakes and GO nanosheets [26] as previously reported.

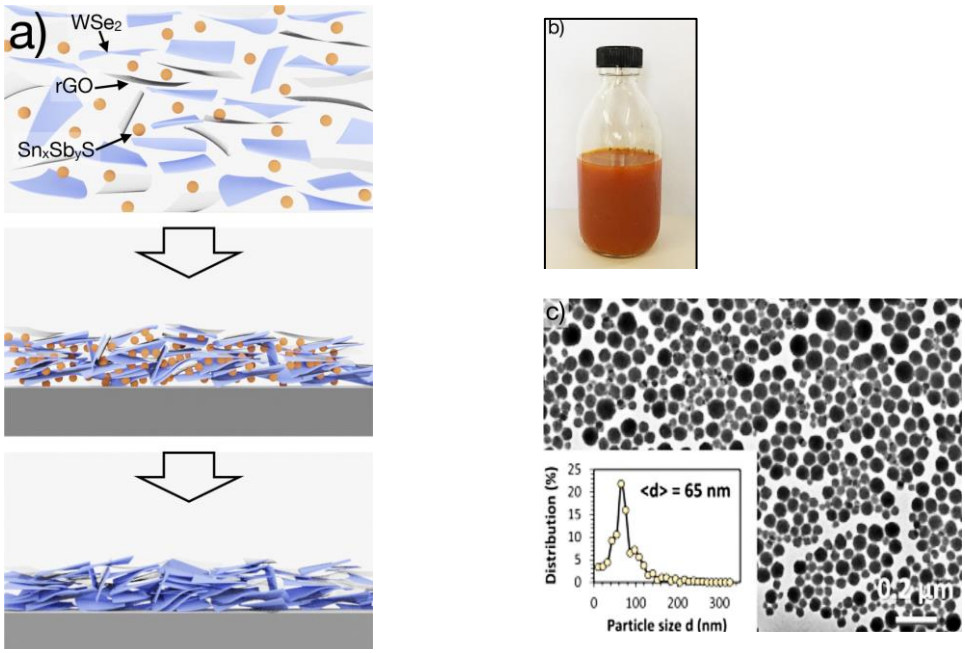

Figure 1: a) Schematic of the co-self-assembly process. b) Photograph of ($Sn_{0.5}Sb_{0.5}S_{1.5}$) template colloidal dispersion in DMF c) TEM image showing monodisperse spherical ($Sn_{0.5}Sb_{0.5}S_{1.5}$) colloids.

To improve percolation of the rGO network, additional infiltration of GO nanosheets was performed by drop-casting mixed solutions containing in addition to the co-textured WSe_2/rGO powder prepared as previously described, free-standing GO nanosheets. After air evaporation, a calcination step was performed at 350 °C (12 h ramp time) under Ar to convert GO into rGO. It is worthy to note that the long duration time of the calcination step improves connection between the WSe_2/rGO co-textured powder thus yielding a nanoporous film composed of layered WSe_2/rGO building blocks. These nanostructured films, denoted hereafter nanostr. WSe_2/rGO films, exhibit r_{rGO} = 0.15. For comparison, two reference films were prepared using i) rGO-free textured WSe_2 powder, denoted nanostr. WSe_2/rGO-free films and ii) exfoliated WSe_2 nanoflakes prepared in similar exfoliation and selection conditions –but without self-assembling- which were simply drop-cast, denoted drop-cast WSe_2 films.

Because WSe_2 nanosheets are sensitive to oxidation, chemical degradation of the nanostructured WSe_2/rGO films prepared from WSe_2 nanoflakes exfoliated in air atmosphere was assessed by X-ray photoelectron spectroscopy (XPS) (Figure S3). From data extracted from the W 4f (WSe_2, B.E.: 31.7; 33.7 eV) and Se 3p regions, we determine Se/W_{molar}= 2, indicating absence of significant WSe_2 degradation. A more quantitative value of the oxidation ratio, $r_{W..O}$ = W..O / (W..O + W..Se), $r_{W..O}$ = 0.135, was extracted from 4f 7/2, 4f 5/2, tungsten oxide (WOx) peaks (B.E.= 35.3 and 37.4 eV, [33-34]) confirming a low oxidation ratio. Because a similar value of $r_{W..O}$ was observed on freshly exfoliated WSe_2 nanoflakes, the observed slight oxygen contamination thus mainly arises from the exfoliation process performed in air atmosphere. This result also demonstrates that no significant chemical oxidation of the WSe_2 nanoflakes occurs during the whole co-self-assembly process including the GO thermal reduction step when using WSe_2 building blocks selected at 800 rpm. ~~From XPS data, a WSe_2 oxidation ratio [31-32], W_{ox}, W_{ox} = W..O/(W..O + W..S)$_{molar}$ of 0.13 mainly arising from the exfoliation process (see Supp info) was determined on the nanostructured WSe_2/rGO film prepared from exfoliated WSe_2 nanoflakes and selected at 800 rpm.~~ Importantly, the cyclic voltammetry curves recorded on the nanostr. WSe_2/rGO-free film prepared from WSe_2 nanoflakes selected at 800 rpm show an enhancement of the electrochemical surface area. A 4-fold increase of the capacitance compared to the drop-cast photo-electrode is observed revealing a remarkable improvement of the electrochemically accessible surface area with nanostructuration (Figure 2).

Typical cross-section SEM image of the nanostr. WSe_2/rGO film (Figure 2a) was recorded at relatively low magnification after sequential slicing using FIB milling. We can clearly observe a porous skeleton composed of interconnected building blocks displaying anisotropic morphology. Presence of W and Se shown by EDS analysis in these anisotropic building blocks demonstrate that these building blocks could be fully identified as WSe_2 nanoflakes. Fine inspection of this SEM image reveals that the photoactive film contains bundles of WSe_2 nanoflakes of average lateral dimension, L= 400 nm, and thickness, e= 100-120 nm, each bundle being composed of an in-plane stacking of ~ 3 primary nanoflakes of ~ 40 nm thickness (Figure 2b). Consistently with this thickness value determined from a small probed volume, a similar thickness value was calculated from the experimentally determined BET surface area of 7 $m^2 g^{-1}$ (Details in Figure S2). Moreover, from an in-depth X-ray investigation and using a Williamson-Hall model [35], two sets of data are clearly observed yielding two different plots resulting from the anisotropic morphology of the ordered domains (Figure S4). As expected, larger ordered domain size is observed for the diffraction peak of the (00l) basal plane. More important, the ordered domain size determined for the (100), (105) diffraction peak (e= 46 nm) is in line with the primary building blocks thickness of the WSe_2 nano-flakes determined from SEM picture (Figures 2a, 3a). ~~X-Ray ordered domains of ~ 45-50 nm were determined for the (100), (105) directions (Figure S4).~~ These values determined on a nanostructured film free from preferential orientation indicate that these primary nanoflakes were indeed monocristalline. The intimate mixture of rGO nanosheets and WSe_2 nanoflakes is illustrated on Figure 2c showing a rGO nanosheet coating the WSe_2 nanoflake. Although the partial extension of the rGO nanosheet beyond the WSe_2 nanoflake was clearly observed, thus favoring the formation of a percolated network of rGO nanosheet till the back FTO electrode, several clues confirm that the WSe_2 nanoflakes are intimately coated by the rGO nanosheets. First, nanostructured WSe_2 powders prepared with and without rGO were shown to display nearly similar pore volume, pore distribution and BET surface area (Figure S2a,b). In addition, although slightly lower, a similar order of magnitude for the electrochemically active surface was determined by voltammetry (C-V curves, Figure 2e) in 0.5 M H_2SO_4 on the nanostructured WSe_2/rGO photo-electrodes prepared from the co-textured WSe_2/rGO powder compared with a reference nanostructured rGO-free WSe_2 powder. Taking in account that the rGO ratio incorporated into the film is lower than the amount required for the full coverage of the WSe_2 nanoflakes surface (Figure S2), all these

results indicate a patch-like coating of the WSe_2 surface by the rGO nanosheets rather than the presence of a high proportion of free-standing rGO.

3.2. Decrease of charge carrier accumulation by construction of a percolated rGO nanosheets network.

In contrast to drop-cast reference films displaying a large number of plane-to-plane contacts, the majority of contacts observed in the cross section image of the nanostructured films composed of 2D nanoflakes are edge-to-plane or edge-to-edge contacts (Figure 2a). More specifically, the large decrease of plane-to-plane contacts should greatly affect the electrical conductivity of the film. As expected, significant decrease of the lateral conductivity over a large distance (1.6 mm) was observed on nanostructured WSe_2 films for measurements performed in Air atmosphere using a four-electrode set-up on WSe_2-Glass films (Figure 2f). The better conductivity of the reference drop-cast film indicates reasonable long-range conductivity in the range of 10^{-2} S m^{-1} resulting both from the in-plane conductivity of the primary WSe_2 nanoflakes [36] and from the higher number of plane-plane contacts into these films. In contrast, in the nanostructured WSe_2 film displaying mainly edge-to-plane or edge-to-edge contacts, the significant electrical conductivity decrease down to 10^{-4} S.m^{-1} highlights the poor electrical connectivity of these contacts. Interestingly, although the rGO nanosheets produced from thermal reduction of ultra-sonicated GO were not well-crystallized, the long range electrical conductivity was restored within the nanostr. WSe_2/rGO film by insertion of a low rGO concentration (0.72 % wt rGO or r_{rGO}= 0.2).

Using a co-self-assembly process, this result demonstrates the formation of a percolated network of rGO nanosheets occurring at a rGO/WSe_2 surface coverage ratio σ= 0.85 (for details, Figure S2). Similarly, ~~Linear Scanning Voltammetry~~ LSV curves recorded on the nanostr. WSe_2/rGO films also show higher photocurrents for an optimal rGO ratio at r_{rGO}= 0.2 (Figure 2g) in H_2SO_4 0.5 M. More insights into the rGO contribution were gained from electrochemical impedance spectroscopy (EIS) measurements. The lower resistance values extracted from the low frequency range of the Nyquist plots are observed at a similar optimal ratio, r_{rGO}= 0.20 (Figure 2g). Because these low frequency data are associated to the semiconductor-electrolyte interface [37,38], this indicates an improved charge transfer at this interface occurring simultaneously with the net decrease of the charge carrier

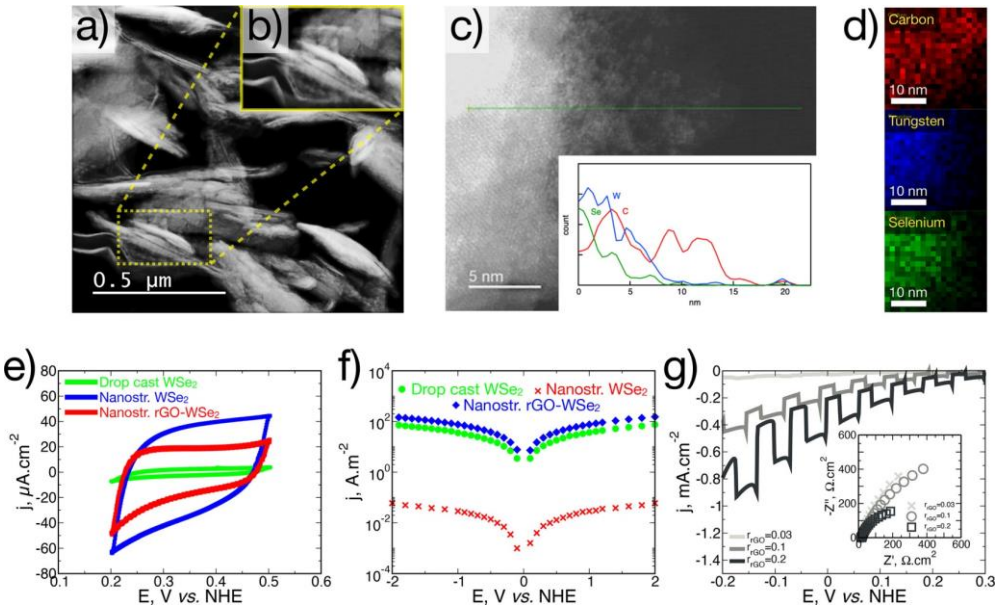

Figure 2: WSe_2/rGO nanostructured 2D photocatalyst properties. a) FIB-TEM cross section image showing a percolating network of WSe_2/rGO nanoflakes displaying mainly edge-edge or edge-plane contacts. b) Insert: Zoom showing that the 120 nm thick, WSe_2 bundle is composed of 3 primary nanoflakes of ~ 40 nm. c) TEM image showing a rGO nanosheet covering a WSe_2 nanoflake. W, Se and C EELS spectra showing a rGO nanosheet stretching out outside the WSe_2 surface over 5 nm. d) Carbon, tungsten and selenium mapping showing coating of WSe_2 by rGO. e) Capacitance –Voltage (C-V) curves recorded at 20 mV/sec in 0.5M H_2SO_4 for the rGO-free/WSe_2 and rGO/WSe_2 nanostructured films. Comparison with the C-V curve recorded on drop-cast WSe_2 reference film, given for reference highlights the high electrochemical accessible surface area for the rGO-free/WSe_2 and rGO/WSe_2 nanostructured photo-catalysts. f) In-plane electrical conductivity of nanostructured 2D rGO/WSe_2 and WSe_2 films. Data collected from a drop-cast WSe_2 film is also given for reference. g) LSV curves showing r_{rGO} ratio dependence of photo-current. Insert: Dark EIS plots of corresponding films showing decrease of charge transfer resistance with r_{rGO} ratio. H_2SO_4 0.5 M. E= -0.2 V vs NHE.

accumulation and recombination resulting from the formation of the percolating conducting network in the photoactive film (Figure 2f,g). All these results highlight the crucial importance of improving charge carrier transport within high surface area, nanoporous photo-electrodes composed of 2D building blocks. Effects of nanostructuration implemented to the patch-like hetero-structures are demonstrated from the significant differences observed on typical LSV curves recorded on drop-cast and nanostructured WSe_2/rGO photo-electrodes after rGO ratio optimisation (Figure S5).

3.3. Catalytic activation of the 2D photocatalyst by a multicomponent ultrathin film.

To fully benefit from the unique properties displayed by the architectured 2D WSe_2 photo-catalyst, an ultrathin film of healing catalyst was designed to coat intimately the rGO-partially-coated WSe_2 nanoporous skeleton. Use of a multicomponent layer capable of both healing the WSe_2 surface defects and displaying a high catalytic activity [6] favours the formation of more homogeneous hetero-structures possessing more uniform thickness. To preserve the small mean free-path of charge carriers relevant to these layered nanostructures, it is mandatory to efficiently passivate and catalytically activate the photo-electrode with a film thickness as thin as possible. In this context, the formation of a continuous ultrathin film was thus explored at ambient temperature in a heterogeneous growth regime from a large variety of diluted aqueous Mo sulfide complexes solutions (Mo= 0.01 M, $4 \leq S/Mo \leq 6$, $8.0 \leq pH \leq 9.7$).

Best photocatalytic performances were achieved by deposition of an ultrathin film performed in low supersaturation conditions (0.01 M Mo) from a distribution of Mo sulfides complexes formed spontaneously in H_2O and prepared at pH 9 and S/Mo= 5. In addition to the thio- and oxo-thio- Mo monomers species such as $(MoS_4)^{2-}$, $(MoOS_3)^{2-}$, an electro-spray ionization mass spectrometry (ESI-MS) investigation (Figure S6) reveals that these solutions display peak concentrations of highly catalytically active dimers $(Mo_2S_{12})^{2-}$ [39], $(Mo_2S_6O_2)^{2-}$ [40] and trimers $(Mo_3S_8O)^{2-}$. Formation of a stable, ultrathin film displaying high photo-electrochemical performances was achieved using a selective dip coating process including successive long duration time (up to 2x 16 h) alternating with H_2O washings [6].

Typical cross-section SEM image the co-catalyst /WSe_2/ rGO hetero-structures was recorded after sequential slicing (Figure 3a) using a FIB. We can clearly observe a porous skeleton composed of interconnected building blocks displaying an anisotropic morphology. Interestingly, consistently with XRD data (Figure S4a), ~~the observation~~ presence of random orientations of the WSe_2 nanoflake building blocks indicates a successful 3D self-assembly. Fine inspection of the interconnected network reveals the presence of irregular contours on the periphery of nanoflakes and curved domains at inter-nanoflakes junctions. This indicates the presence of a continuous film coating the WSe_2 nanoflakes. Although the accurate determination of the average thickness of the WSe_2 nanoflakes remains difficult from the SEM images, the WSe_2 nanoflakes exhibit an average thickness around ~ 120 nm, close to the average thickness previously determined on the catalyst-free WSe_2/rGO nanostructures. Careful observation of the SEM images also reveals the presence of higher contrast linear

domains all along the co-catalyst/WSe_2/rGO skeleton confirming as previously observed on the nanostr. co-catalyst-free/WSe_2/rGO film that these anisotropic hetero-structures of ~ 120 nm thick are indeed mainly composed of the stacking of ~ 3 primary nanoflakes (Insert Figure 3a). Note that from an in-depth inspection of the sample, we cannot discard the presence of isolated WSe_2 nanoflakes of lower thickness. For example, better illustration of the properties of the co-catalyst/WSe_2 interface was performed on isolated nanoflakes of lower thickness (~ 8 nm thickness composed of ~ 12 elementary nanosheets) coated by an ultrathin film of co-catalyst (Figure 3b). From EDS analysis, both the nanoflakes as well as the lower contrast domain coating the nanoflakes were fully identified as WSe_2 and co-catalyst with the respective presence of W, Se and Mo, S. Figure 3b reveals the formation onto the WSe_2 surface of a homogenous, compact and perfectly adherent co-catalyst coating. Electronic diffraction performed on this coating clearly demonstrates its amorphous feature. A high resolution STEM image taken at a nanometer scale (Figure 3c) reveals that the Van der Waals layered structure remains largely intact with an interlayer spacing of 0.66 nm which is within 0.5 % of the one reported for bulk WSe_2 [41]. More important, the HRTEM image also shows that the layered structure of the WSe_2 is preserved up to the WSe_2 nanoflake periphery after co-catalyst deposition without any diminishing in lateral size, clearly demonstrating that no degradation occurs at the edges of the WSe_2 nanoflakes as shown in Figure 3c. Details of the Mo_xS_y/WSe_2/rGO hetero-structure is provided by high resolution STEM-EDS mapping. The HAADF image (Figure 3d) shows a WSe_2 nanoflake of 12 nm thickness composed of ~ 16 elementary nanosheets in a cross-section view where the elementary nanosheets can be observed by contrast. As expected, STEM–EDS mapping reveals the presence of a ~ 12 nm core containing the W, Se elements. Although our co-self-assembly process favors the formation of 2D/2D, WSe_2/rGO planar interfaces, the coating of the WSe_2 nanoflake edges by rGO nanosheets has also been observed as shown from Carbon STEM–EDS mapping. This unambiguously demonstrates the presence of rGO in our hetero-structures. In addition, STEM-EDS mapping analysis of Mo and S clearly shows the presence of Mo and S on the periphery of the WSe_2 nanoflake. Consistently with the post-deposition of an ultrathin (1 to 2 nm thick) Mo_xS_y film onto the WSe_2/rGO nanostructured film, the WSe_2 nanoflake is sandwiched between two ultrathin layers of co-catalyst. This is an experimental evidence of the formation of the layered anisotropic hetero-structure spatially distributed according to the well-defined sequence Mo_xS_y/WSe_2/rGO (Figure 3d).

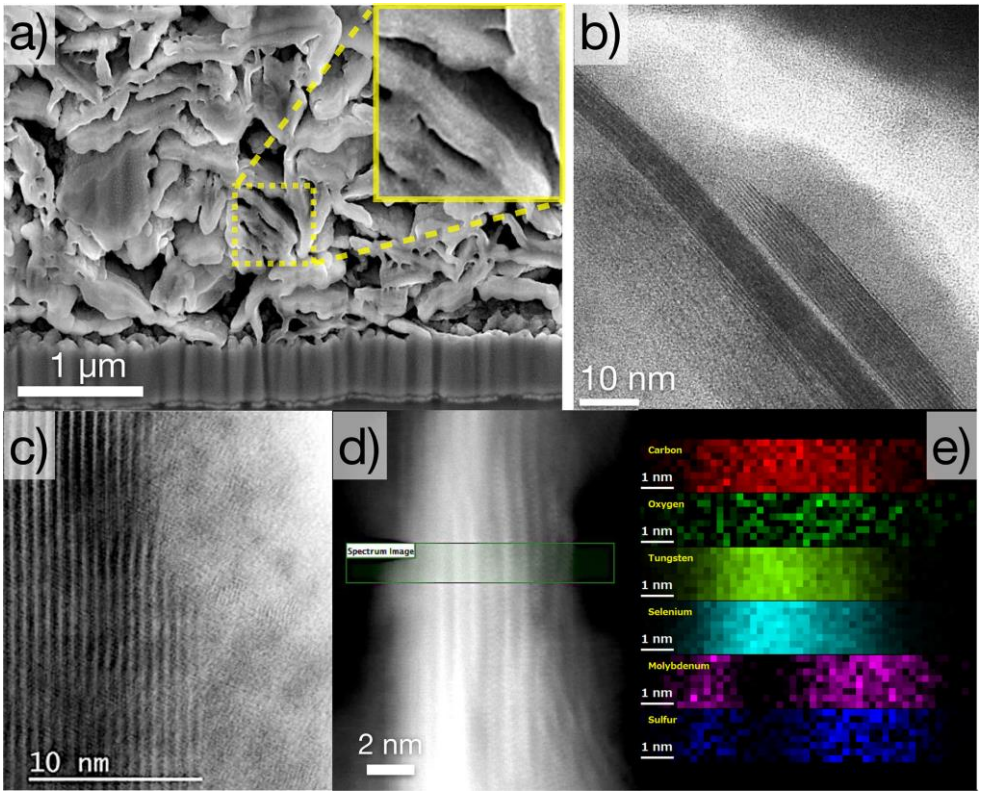

Figure 3. Properties of co catalyst/WSe_2/rGO photo-electrodes. a) FIB-SEM cross section image showing an interconnected 3D porous assembly of WSe_2 anisotropic nanoflakes. Insert: Zoom showing presence of higher contrast linear domains all along the 120 nm thick co-catalyst/WSe_2 skeleton highlighting the stacking of 3 nanoflakes. b) High Resolution TEM image showing WSe_2 nanoflakes embedded in amorphous Mo_xS_y co-catalyst. c) HRTEM image at the nanoscale demonstrating no degradation at the edge of a WSe_2 few-layer after co-catalyst deposition. d, e) Atomic-resolution HAADF-STEM image showing the detailed structure at the nanometer scale of the Mo_xS_y/WSe_2 layered hetero-structure**.** The ~ 5 nm thick WSe_2 nanoflake is sandwiched between an ultrathin, co-catalyst film of ~ 2 nm Mo_xS_y.

Note that extension of rGO nanosheets outside the WSe_2 nanoflake has been also observed. On another HAADF–STEM –EDS image, Figure S7 depicts a 40 nm thick WSe_2 nanoflake together with an rGO nanosheet spreading out 60 nm from the WSe_2 nanoflake in a non-coiled conformation. All these results indicate the successful formation of a nanoporous skeleton formed from 120 nm thick, tri-layer hetero-structure building blocks composed of co-catalyst ultrathin film, WSe_2 nanoflake and rGO nanosheet.

Chemical composition of the ultrathin co-catalyst film was probed by XPS analysis. Because of the porous structure of the film and of the low average thickness (e_{cc} < 10 nm) of the co-catalyst film, XPS can be used to provide quantitative data of the chemical composition of

the whole co-catalyst film as well as of the WSe_2 nanoflake surfaces. From the data extracted from the Mo 3d and the S 2p regions and using assignments previously reported in the literature [42], an average value of S/Mo_{molar}= 4.5 was determined for co-catalyst film withdrawn after the first hours of dip coating (5 h dip coating). Importantly, films displaying high photo-electrochemical performances and prepared at longer dip coating time (2x 16 h), exhibit a significant increase of S/Mo ratio to S/Mo= 5.2 (Figure S3). Changes observed in the S/Mo ratio during the growth of the co-catalyst film probably result from different growth mechanisms. In a first step, deposition of thio-, oxo-thio- Mo complexes may be driven by adsorption energies on the bare WSe_2 while coordination–reticulation may later dictate the film growth process. The S/Mo value determined on our co-catalyst film compared with previously reported data [43,44] suggests the presence in high proportions of $(Mo_2S_{12})^{2-}$ species displaying both high catalytic activity [39] ~~and high S/Mo ratio,~~ in association with species displaying lower small S/Mo ratios such as $(MoOS_3)^{2-}$, $(Mo_2S_6O)^{2-}$ and $(MoS_4)^{2-}$.

3.4. Healing and optoelectronic properties of the co-catalyst ultrathin film.

The healing properties of the co-catalyst film were first demonstrated by a photoluminescence investigation (Figure 4a). ~~Photoluminescence~~ PL measurements on the nanostr. catalyst-free/WSe_2/rGO films reveal no measurable luminescence as a consequence of the high concentration of electronically active surface defects usually present in these 2D materials. In contrast, despite bulk WSe_2 is known to display poor luminescence due to its indirect nature of the band gap, luminescence signals were clearly recorded for measurements performed on the Mo_xS_y/WSe_2/rGO hetero-structures. Figure 4a shows the

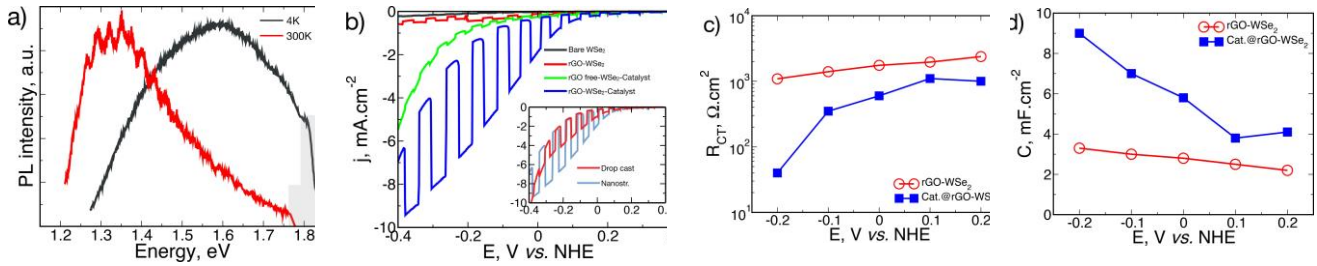

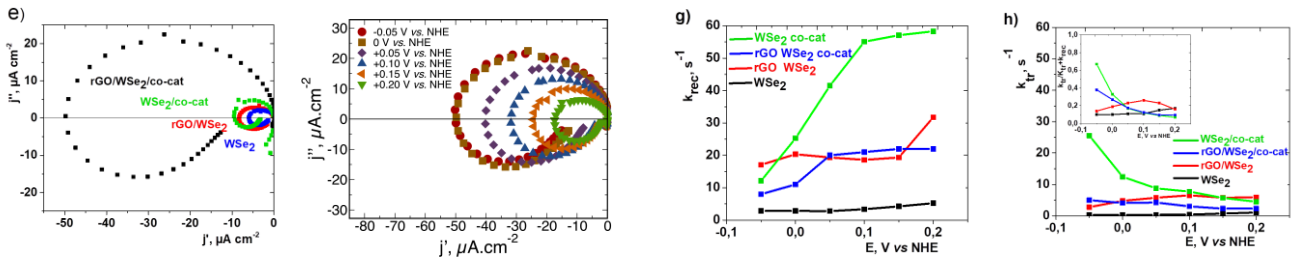

Figure 4: Healing properties of the Mo_xS_y co-catalyst ultrathin film. a) Normalized PL of co-catalyst coated 2D WSe_2 photo-catalyst at 4 K and 300 K. b) LSV curve recorded on Mo_xS_y coated-nanostructured 2D WSe_2 photo-catalyst showing beneficial effect of nanostructuration. LSV curves on various reference photo-electrodes are given for comparison. Insert: LSV curves recorded on drop-cast (reference) and nanostructured co-catalyst coated/WSe_2 photo-electrodes. c) Charge transfer resistances R_{CT} and d) Capacitances fit from impedance responses of bare and co-catalyst coated WSe_2/rGO nanostructured photo-electrodes under illumination (λ= 450 nm), H_2SO_4 0.5 M, E= -0.1 V vs NHE. e) IMPS spectra of WSe_2-based photo-electrodes, E= 0.0 V vs NHE. Electrolyte H_2SO_4 0.5 M. λ = 680 nm. f) IMPS spectra of co-catalyst/WSe_2/rGO photo-electrode. Electrolyte H_2SO_4 0.5 M. λ = 680 nm. g) Recombination rate constants and h) Charge transfer rate constants for WSe_2-based photo-electrodes. Insert Fig. 4h: Zoom showing increase of charge transfer efficiency ($\eta_{ct} = k_{tr}/(k_{tr} + k_{rec})$) with polarization for co-catalyst coated/WSe_2 nanostructured photo-electrodes.

wavelength shift of the PL emission peak-position from ~909 nm (1.36 eV) at 300 K to 780 nm (1.59 eV) at 4 K exciting the sample with the red line of a He-Ne laser ($\lambda = 632.8$ nm) with a power of 500 µW. While the position of the PL peak of the room temperature photoluminescence could be interpreted as an envelope including mainly building blocks formed from several nanoflakes with an average thickness around 20 - 45 nm [45-46], the measurement of a sizeable PL intensity in these multilayer structures indicates the successful mitigation of defect-mediated non-radiative recombination and clearly demonstrates passivation of surface defects.

In addition to the surface defects passivation, the co-catalyst film exhibits semi-conduction as demonstrated by UV-Vis spectroscopy (Figure S8). From Mott-Schottky analysis, we have shown the n-type semi-conduction and determined the flat band potential of the co-catalyst film. Interestingly, in combination with the p-character of the WSe_2 nanoflakes (Figure S8), the n-Mo sulfide co-catalyst ultrathin film was shown to build a beneficial p/n junction [47].

3.5. Increasing photo-electrochemical performances of the 2D photocatalyst by nanostructuration.

Performance improvements resulting from the nanostructuration are clearly shown on the LSV curves (Figure 4b) recorded on films prepared at r_{rGO}= 0.15 using WSe_2/rGO co-textured powder in combination with a GO nanosheets post-addition. Compared with photocurrents recorded on reference photo-electrodes fabricated from drop-cast exfoliated-WSe_2 nanoflakes or nanostr. rGO-free/WSe_2 films, a remarkable large average photocurrent up to j= 5 mA cm^{-2} at -0.2 V / NHE (on six replicate electrodes tested) in the range of the best values of the state of the art for photoactive 2D WSe_2 electrodes [23] was recorded under intermittent 1 sun illumination on the co-catalyst/WSe_2/rGO-hetero-structures. While no thickness dependence was observed for the rGO-free films, it is worth noting that the larger photocurrents were achieved on relatively thick rGO/WSe_2/co-catalyst films (e= 4 µm). Using the hetero-structuration strategy developed in this work, an optimal thickness of 4-5 µm was determined for our 2D nanoporous film yielding a 3-fold increase of the photocurrent density.

To demonstrate that the recorded photocurrent could be ascribed to the hydrogen formation, we have measured the real-time hydrogen evolution by gas chromatography (Figure S9). Under continuous illumination, evolved H_2 gas was measured and compared to a Pt calibration curve. A Faradic yield around 95 % was determined indicating proton reduction as the main reaction. Moreover, another important criterion is film stability. The chrono-amperometric behaviour of the catalyst/WSe_2/rGO photo-electrode in 0.5 M H_2SO_4 is reported Figure S10 showing a nearly constant photocurrent observed under intermittent illumination demonstrating photo-electrode stability. In addition, no significant evolution was observed on the Raman spectra and TEM images recorded before and after HER testing. Although the co-catalyst film was formed from water-soluble Mo complexes, all these results are consistent with the formation of a partially well-reticulated, stable, co-catalyst film.

Incident-photon-to-current efficiency (IPCE) measurements were performed illuminating the photocathode using a set of high-power light emitting diodes (Figure S11). The better IPCE value was determined at λ= 760 nm with IPCE= 13.2 %. Although a better photon absorption is measured (Figure S11) in the WSe_2 film over the wavelengths range 400-600 nm, as shown from the absorbance spectrum, lower IPCE values (10 % at λ= 515 nm) are determined at shorter wavelengths.

3.6. Effect of coverage ratio of the WSe_2 nanoflakes by rGO and MoxSy film on charge transfer and surface recombination.

In addition to the LSV curves previously reported, an electrochemical impedance spectroscopy investigation (Figure S12) under illumination (λ= 450 nm) clearly reveals a lower charge transfer resistance along with a higher capacitance observed for the co-catalyst coated Mo_xS_y/WSe_2/rGO photo-electrode compared with the bare one (Figure 4c,d). For regular electrochemical processes under charge transfer control, the current is expected to vary exponentially with polarisation as observed for the bare sample (Figure 4c). This is not the case for the coated one indicating a better charge separation and collection for this sample. Thus, in contrast to the regular exponential charge transfer dependence, the more efficient charge separation and longer minority charge carrier lifetime achieved for the coated Mo_xS_y/WSe_2/rGO sample allow the building up of a larger interface charge concentration and a higher capacitance (Figure 4d). In addition to highlight the increase of the effective charge transfer surface site number, the capacitance increase can also be interpreted as a clear evidence of charge accumulation throughout the co-catalyst film. Indeed, several authors [37] have proposed that the capacitance increase could be assigned to the transfer of photo-generated charge carriers to the co-catalyst layer instead of being trapped in surface states of the photoactive material. In this interpretation, the charge carrier accumulation may imply a redox reaction involving the formation of intermediate species within the co-catalyst film such as unsaturated Mo(IV) sites which were furthermore previously identified as catalytically ready species. In addition, because these intermediates are subjected to recombination by oxidation, the observed increase of capacitance with polarization could be explained by hindered recombination with applied potential and band bending. Despite a partial coverage of the WSe_2 surface by the rGO nanosheet hindering the passivation of a proportion of in-plane surface defects, these results unambiguously demonstrate the beneficial effect of the co-catalyst film on improving the electron transfer as well as lowering the surface recombination.

Because EIS investigation of the semiconductor/electrolyte interfaces involves a potential variation to modulate the whole reaction rate, this technique does not allow to deconvolute the surface recombination and charge transfer processes. Better insight into the overall effective charge transfer resistance, i.e. deconvolution of the dark and photocurrent, can be obtained by intensity modulated photocurrent spectroscopy (IMPS) [48] allowing

modulation of one reactant, i.e. the surface concentration of photo-generated carriers. Typical IMPS complex plots recorded in H_2SO_4 0.5 M on non-coated and co-catalyst coated WSe_2/rGO nanostructured photo-electrodes are reported Figure 4e,f and Figure S12. The IMPS reference curves determined on drop-cast, non-coated and co-catalyst coated rGO-free, WSe_2 photo-electrodes are also given for comparison (Figure S12-4). Except for the co-catalyst/WSe_2/rGO photo-electrode, all the photo-electrodes (WSe_2, WSe_2/rGO and co-catalyst/WSe_2) exhibit low frequency intercepts indicating, consistently with the photocurrents recorded on the LSV curves, a small fraction of the photocurrent injected into the electrolyte even at high cathodic potential. Inspection of these IMPS curves also reveals a low dependence of the Nyquist curves with applied potential observed for the WSe_2 photo-electrode. In contrast, a different behaviour is observed for the co-catalyst coated photo-electrodes. Particularly, the co-catalyst/WSe_2/rGO photo-electrode shows a much more potential dependent high frequency intercept together with a larger fraction of photo-generated electrons that reach the semiconductor/electrolyte interface. This notable difference, in agreement with the J –V curve (Figure 4b) recorded on the nanostructured WSe_2/rGO photo-electrode after co-catalyst deposition, probably results from the p/n junction formation following the co-catalyst deposition. Figure 4g,h depicts the charge transfer (k_{tr}) and the recombination (k_{rec}) rates extracted from these plots. While a reasonable increase of k_{tr} values was determined with applied cathodic potentials for the non-coated, rGO-free, WSe_2 photo-electrode, deposition of the co-catalyst film yields as expected larger values of k_{tr} in the whole range of applied potentials. More important, IMPS data also clearly reveal that the addition of rGO significantly decreases the k_{tr} values. As previously observed from the HRTEM images, this could be attributed to the partial coverage of the WSe_2 nanoflake surfaces by the rGO nanosheets thus diminishing the WSe_2 electrochemically active surface area. It is worth noting that this partial coverage of the photoactive WSe_2 surface by the rGO nanosheets was achieved for an incorporated r_{rGO} ratio (r_{rGO}= 0.15) which corresponds to an equivalent surface coverage ~0.64. Note that this value is probably overestimated due to the presence of some rGO nanosheets of larger size extending out from the WSe_2 surface as shown from the TEM images (Figure S7). Another key point extracted from these IMPS curves is the large values of k_{rec}. The larger values of k_{rec} observed for the co-catalyst coated WSe_2 photo-electrode probably arise both from the non-favourable band offset displayed by the co-catalyst band conduction level against the

hydrogen evolution potential and from hindered hole transport to the back electrode. Consistently, a significant and favourable evolution of the k_{rec} values is observed either with applied cathodic potentials or after rGO insertion into the co-catalyst coated WSe_2 photo-electrode. Although the rGO-containing WSe_2/co-catalyst photo-electrode displays lower k_{rec} values compared with the rGO-free, WSe_2/co-catalyst photo-electrode, nearly similar charge transfer efficiency values ($\eta_{CT}= k_{tr}/k_{tr}+k_{rec}$) were extracted from the IMPS curves.

Our results show that the partial coating of the WSe_2 photoactive material by the rGO nanosheets does not significantly alter the charge transfer efficiency of the WSe_2 photo-electrode. Despite the loss of photoactive surface area caused by the rGO shielding, the patch-like hetero-structuration strategy developed in this work proves to significantly increase the performances of the 2D photo-electrodes. This reveals that this loss is larger compensated by the surface area gain achieved by the mass loading increase resulting from the rGO addition.

3.7. Healing properties by thio-, oxo-thio-Mo monomers adsorption on WSe_2 edge defects.

2D materials are known to display a large concentration of defects. These defects were mainly identified as in-plane (or internal) point defects including W or Se vacancies [49,50] especially for WSe_2 nanosheets of low thickness, i.e. e < 4 nm. For WSe_2 nanoflakes possessing a higher thickness (e= 45-70 nm), edge defects become more important, making crucial interactions between edge defects and oxo-thio-Mo- complexes. To get better insights into the effect of MoxSy co-catalyst film on the passivation of the WSe_2 photo-electrode, adsorption energies of thio-, oxo-thio-Mo monomers $(MoOS_3)^{2-}$ and dimers $(Mo_2S_{12})^{2-}$ forming the co-catalyst layers were thus determined from DFT calculations. Because the edge defects were predominant in our nanoflakes, we first focused on adsorption modes (coordination and energies) of oxo-thio-Mo complexes on edge defects of a WSe_2 nanoflake.

Our model, built like any slab, from a 2H WSe_2 bulk system, see Supplementary Information for the computational details, exhibits few distinct adsorption sites, after a strong edge reconstruction, as it can be seen in Figure S13. Indeed upon geometry optimization, the two edges presenting W-termination reconstruct themselves to always present Se-terminations.

To investigate the adsorption modes of the molecular complexes we have used their radical form, to avoid the complexity of studying charged species in periodic boundary conditions. From these series of calculations, the $MoOS_3^{2-}$ complex was shown to display high adsorption energies towards the edge defects, around -4.83 to -5.51 eV depending on the coordination mode, while the adsorption energies for $(Mo_2S_{12})^{2-}$ complex are much weaker, from -0.66 eV to -0.84 eV. The most stable adsorption modes of $(Mo_2S_{12})^{2-}$ and $(MoOS_3)^{2-}$ complexes on these edge defects are given in Figure 5. This suggests that passivation of edge

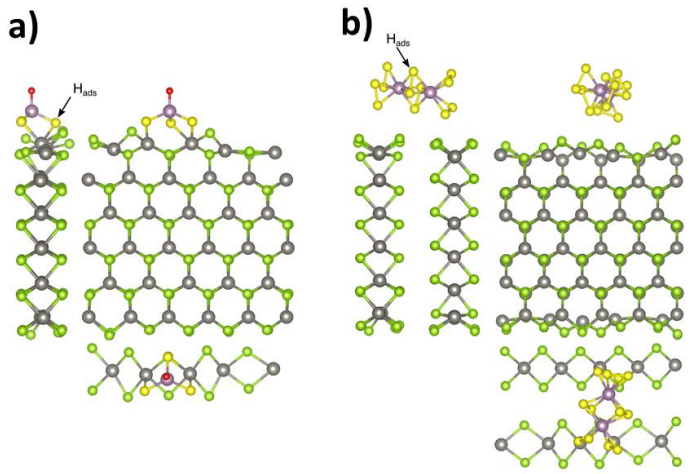

Figure 5. Side views (a) and top views (b) of the most stable adsorption modes for $(MoOS_3)^{2-}$ in the left panel and $(Mo_2S_{12})^{2-}$ species in the right panel. Se atoms are in green, W in gray, S in yellow, O in red, when Mo atoms are in black. Black arrows correspond to the most stable coordination for a H atom.

defects probably results from the strong adsorption of the smaller molecular complexes on the edges. Moreover, these edge defects strongly adsorbed by the small thio-, oxo- thio-Mo-complexes probably act as nucleation sites thus favoring the formation of a continuous highly adherent coating of catalyst by chemical deposition.

With the findings of the most stable H-adsorption configurations for the two deposited Mo-based complexes, as given in Figure 5, one can estimate their corresponding ΔG_H [51]. Interestingly the adsorption of an H species on an adsorbed $(MoOS_3)^{2-}$ gives a ΔG_H of 0.66 eV while it is -0.26 eV for $(Mo_2S_{12})^{2-}$. Although good catalytic activity for this Mo-dimer was

previously reported in the literature in its free-standing form [37], our calculations show better catalytic performance of the $(Mo_2S_{12})^{2-}$ dimer -vs $(MoOS_3)^{2-}$ monomer- in their anchored configurations. Thus, DFT calculations clearly suggest that small complexes with low S/Mo ratio are strongly adsorbed and act as healing additives while polynuclear complexes such as $(Mo_2S_{12})^{2-}$ display catalytic activity. It is worth noting that these later complexes were shown by XPS to be localized at the film periphery in contact with the electrolyte.

Our patch-like hetero-structures exhibit 2D/2D, WSe_2/rGO interfaces achieved from a co-self-assembly process. Partial coverage of the photoactive WSe_2 nanoflake surfaces was tuned by use of rGO nanosheets of lower lateral size and control of the rGO addition ratio. As a result, the partial coating of the WSe_2 surface by the rGO nanosheets yields a proportion of non-healed, in-plane surface defects. Despite the presence of these non-healed, in-plane defects, our hetero-structuration strategy was proven to be efficient. This may result both from i) the relatively large thickness of the WSe_2 nanoflakes exhibiting a larger population of edge rather than in-plane defects ii) The favored injection of carrier into the electrolyte to achieve HER via these edge sites. Indeed, the photo-generated charge carriers flow preferentially through the in-plane direction as a result of its higher electronic conductivity [36,52]. Coating these edge-sites by a healing co-catalyst thus allows passivation of the recombination centers while improving the charge transfer process on neighboring edge sites, yielding a significant increased photocurrent.

4. Conclusions

A new film nanostructure composed of interconnected ultrathin, layered hetero-structures made of WSe_2 nanoflakes, rGO nanosheets and a healing co-catalyst film is proposed. The WSe_2-based nanoporous network was prepared by co-self-assembly of WSe_2 nanoflakes, GO nanosheets of lower lateral size, and post-deposition of a co-catalyst ultrathin film. A resulting patch-like, layered, hetero-structure was achieved with partial coverages of the photoactive WSe_2 surface both by the rGO nanosheets and by the ultrathin film of co-catalyst. Despite the partial shielding by the rGO nanosheets hindering the surface defects

passivation by the healing co-catalyst film, the patch-like hetero-structuration strategy developed in this work proves to significantly increase the performances of 2D photo-electrodes. Good photoelectrochemical properties of WSe_2-based, patch-like hetero-structures were demonstrated with photocurrent densities up to 5 mA cm^{-2} for hydrogen generation. Future research efforts will be devoted to 2D TMDC films with lower thickness with the objective to increase surface area and photocurrent densities. We hope that this new strategy to improve charge transport properties in high surface area, layered hetero-structures will provide a new and exciting opportunity to boost the performances of 2D photoactive materials for energy conversion.

Declaration of competing interest

The authors declare that they have no known competing financial interests or personal relationships that could have appeared to influence the work reported in this paper.

Acknowledgements.

J. B. B. thanks Conselho Nacional de Desenvolvimente Cientifico e Technologico (CNPQ), Brazil, for the financial support through CNPq grants (CNPq 201490/2015-3 and INAMI/CNPq/MCT). J. Esvan is gratefully acknowledged for his help during XPS measurements.

References

[1] A Heller, Hydrogen Evolving Solar cells, Science 223 (1984) 1141-1148.

[2] E. F. Osterloh, Inorganic Nanostructures for Photo-Electrochemical and Photocatalytic Water Splitting, Chem. Soc. Rev. 42, 6 (2013) 2294-2320.

[3] S. W. Boettcher, E. L. Warren, M. C. Putnam, E. A. Santori, D. Turner-Evans, M. D. Kelzenberg, M. G. Walter, J. R. McKone, B. S. Brunschwig, H. A. Atwater, N. S. Lewis, Photoelectrochemical Hydrogen Evolution Using Si Microwire Arrays, J. Am. Chem. Soc. 133 (2011) 1216–1219.

[4] S. C. Warren, K. Voïtchovsky, H. Dotan, C. M. Leroy, M. Cornuz, F. Stellacci, C. Hébert, A. Rothschild, M. Grätzel, Identifying champion nanostructures for solar water-splitting, Nat. Mater. 12 (2013) 842-849.

[5] T. W. Kim, K.-S. Choi, Nanoporous $BiVO_4$ Photoanodes with Dual-Layer Oxygen Evolution Catalysts for Solar Water Splitting, Science 343 (2014) 990-994.

[6] J. Barros Barbosa, P. L. Taberna, V. Bourdon, I. C. Gerber, R. Poteau, A. Balocchi, X. Marie, J. Esvan, P. Puech, A. Barnabé, L. Da Gama Fernandes Vieira, I.-T. Moraru, J. Y. Chane-Ching, Mo thio and oxo-thio molecular complexes film as self-healing catalyst for photocatalytic hydrogen evolution on 2D materials, Appl. Catal. B- Environ. 278 (2020) 119288.

[7] A. Heller, E. Aharon-Shalom, W. A. Bonner, B. Miller Hydrogen-Evolving Semiconductor Photocathodes. Nature of the Junction and Function of the Platinum Group Metal Catalyst, J. Am. Chem. Soc. 104 (1982) 6942-6948.

[8] M. S. Nasir, G. Yang, I. Ayub, S. Wang, L. Wang, X. Wang, W. Yan, S. Peng, S. Ramakarishna, Recent development in graphitic carbon nitride based photo-catalysis for hydrogen generation Appl Catal B- Environ 257 (2019) 117855.

[9] Q. H. Wan, K. Kalantar-Zadeh, A. Kis, J. N. Coleman, M. S. Strano, Electronics and Optoelectronics of Two-Dimensional Transition Metal Dichalcogenides Nat. Nanotechnol. 7 (2012) 699-712.

[10] P. Ganguly, M. Harb, Z. Cao, L. Cavallo, A. Breen, S. Dervin, D. D. Dionysiou, S. C. Pillai, 2D Nanomaterials for Photocatalytic Hydrogen Production, ACS Energ. Lett. 4 (2019) 1687−1709.

[11] T. Su, Q. Shao, Z. Qin, Z. Guo, Z. Wu, Role of Interfaces in Two-Dimensional Photocatalyst for Water Splitting, ACS Catal. 8 (2018) 2253−2276.

[12] J. Jia, W. Sun, Q. Zhang, X. Zhang, X. Hu, E. Liu, J. Fan, Inter-plane heterojunctions within 2D/2D $FeSe_2$/g-C_3N_4 nanosheet semiconductors for photocatalytic hydrogen generation, Appl Catal B- Environ 261 (2020) 118249.

[13] J. Xiong, J. Di, H. Li, Atomically Thin 2D Multinary Nanosheets for Energy-Related Photo Electro-catalysis, Adv. Sci. (2018) 1800244.

[14] M. Q. Yang, Y. J. Xu, W. H. Lu, K. Y. Zeng, H. Zhu, Q. H. Xu, G. W. Ho, Self-Surface Charge Exfoliation and Electrostatically Coordinated 2D Hetero-Layered Hybrids. Nat. Commun. 8 (2017) 14224.

[15] M. Zhou, S. Wang, P. Yang, Z. Luo, R. Yuan, A. M. Asiri, M. Wakeel, X. Wang, Layered Heterostructures of Ultrathin Polymeric Carbon Nitride and $ZnIn_2S_4$ Nanosheets for Photocatalytic CO_2 Reduction. Chem. Eur. *J.* 24 (2018) 18529 – 18534.

[16] K. F. Mak, C. Lee, J. Hone, J. Shan, T. F. Heinz, Atomically Thin MoS_2: A New Direct-Gap Semiconductor, Phys. Rev. Lett. 105 (2010) 136805.

[17] J. R. McKone, A. P. Pieterick, H. B. Gray, N. S. Lewis, Hydrogen Evolution from Pt/Ru-Coated p-Type WSe_2 Photocathodes, J. Am. Chem. Soc. 135 (2013) 223−231.

[18] J. Kang, S. Tongay, J. Zhou, J. Li, J. Wu, Band offsets and heterostructures of two-dimensional semiconductors , Appl. Phys. Lett. 102 (2013) 012111.

[19] H. L. Zhuang, R. G. Hennig, Computational Search for Single-Layer Transition-Metal Dichalcogenide Photocatalysts, J. Phys. Chem. C 117 (2013) 20440−20445.

[20] C. R. Cabrera, H. D. Abruna, Synthesis and Photoelectrochemistry of Polycrystalline Thin Films of p-WSe_2, p-WS_2 and p-$MoSe_2$, J. Electrochem. Soc. 135, 6 (1988) 1436-1442.

[21] J. Hong, Z. Hu, M. Probert, K. Li, D. Lv, X. Yang, L. Gu, N. Mao, Q. Feng, L. Xie, J. Zhang, D. Wu, Z. Zhang, C. Jin, W. Ji, X. Zhang, J. Yuan, Z. Zhang, Exploring atomic defects in molybdenum disulphide monolayers, Nat. Commun. 6 (2015) 6293.

[22] M. Amani, D. H. Lien, D. Kiriya, J. Xiao J, A. Azcatl, J. Noh, S.R. Madhvapathy, R. Addou, K.C. Santosh, M. Dubey, K. Cho, R. M. Wallace, S. C. Lee, J. H. He, J. W. Ager, X. Zhang, E. Yablonovitch, A. Javey, Near-Unity Photoluminescence Quantum Yield in MoS_2, Science 350 (2015) 1065-1068.

[23] X. Yu, N. Guijarro, M. Johnson, K. Sivula, Defect Mitigation of Solution-Processed 2D WSe_2 Nanoflakes for Solar-to-Hydrogen Conversion. Nano Lett. 18 (2018) 215−222.

[24] R. Liu, Z. Zheng, J. Spurgeon, X. Yang, Enhanced photoelectrochemical water-splitting performance of semiconductors by surface passivation layers, Energ. Environ. Sci. 7 (2014) 2504.

[25] V. Agarwala, N. Varghesea, S. Dasguptaa, A. K. Soodb, K. Chatterjeea, Engineering a 3D MoS_2 foam using keratin exfoliated nanosheets, Chem. Eng. J. 374 (2019) 254–262.

[26] M. H. Wahid, X. Chen, C. T. Gibson, C. L. Raston, Amphiphilic graphene oxide stabilisation of hexagonal BN and MoS_2 sheets, Chem. Commun. 51 (2015) 11709.

[27] J. N. Coleman, M. Lotya, A. O Neill, S. D. Bergin, P. J. King, U. Khan, K. Young, A. Gaucher, S. De, R. J. Smith, I. V. Shvets, S. K. Arora, G. Stanton, H. Y. Kim, K. Lee, G. T. Kim, G. S.Duesberg, T. Hallam, J. J. Boland, J. J. Wang, J. F. Donegan, J. C. Grunlan, G. Moriarty, A. Shmeliov, R. J. Nicholls, J. M. Perkins, E. M. Grieveson, K. Theuwissen, D. W. McComb, P. D. Nellist, V. Nicolosi, Two-Dimensional Nanosheets Produced by Liquid Exfoliation of Layered Materials**,** Science 331 (2011) 568.

[28] R. H. Arntson, P. X. Dickson, G. Tunell, Stibnite (Sb_2S_3) Solubility in Sodium Sulfide Solutions, Science 153 (1966) 1673-1674.

[29] M. V. Kovalenko, M. Scheele, D. V. Talapin, Colloidal Nanocrystals with Molecular Metal Chalcogenide Surface Ligands, Science 324 (2009) 1417-1420.

[30] M. V. Kovalenko, M. I. Bodnarchuk, J. Zaumseil, J.-S. Lee, D. V. Talapin, Expanding the Chemical Versatility of Colloidal Nanocrystals Capped with Molecular Metal Chalcogenide Ligands, J. Am. Chem. Soc. 132 (2010) 10085–10092.

[31] Y. Wang, X. Di, X. Gao, X. Wu, P. Wang, Rational construction of Co@C polyhedrons covalently-grafted on magnetic graphene as a superior microwave absorber, J. Alloys

Compd. 843 (2020) 156031-156042.

[32] Y. Wang, X. Di, X. Gao, X. Wu, Design of MOF-derived hierarchical Co@C@RGO composite with controllable heterogeneous interfaces as a high-efficiency microwave absorbent, Nanotechnology 31 (2020) 395710.

[33] P. Biloen, G. Pott, X-ray Photoelectron Spectroscopy Study of Supported Tungsten Oxide, J. Catal. 30 (1973) 169−174.

[34] W. Jaegermann, D. Schmeisser, Reactivity of Layer Type Transition Metal l Chalcogenides towards Oxidation, Surf. Sci. 165 (1986) 143−160.

[35] W.H. Hall, X-ray line broadening in metals, Proc. Phys. Soc. Sect. *A* 62, 11 (1949) 741–743.

[36] Y. Jung, J. Shen, Y. Liu, J. M. Woods, Y. Sun, J. J. Cha, Metal Seed Layer Thickness-Induced Transition From Vertical to Horizontal Growth of MoS_2 and WS_2, Nano Lett. 14 (2014) 6842−6849.

[37] B. Klahr, S. Gimenez, F. Fabregat-Santiago, J. Bisquert, T. W. Hamann, Photoelectrochemical and Impedance Spectroscopic Investigation of Water Oxidation with "Co−Pi"-Coated Hematite Electrodes, J. Am. Chem. Soc. 134 (2012) 16693−16700.

[38] J. H. Kim, S. Han, Y. Hyun Jo, Y. Bak, J. S. Lee, A precious metal-free solar water splitting cell with a bifunctional cobalt phosphide electrocatalyst and doubly promoted bismuth vanadate photoanode, J. Mater. Chem. A 6 (2018) 1266-1274.

[39] Z. Huang, W. Luo, L. Ma, M. Yu, X. Ren, M. He, S. Polen, K. Click, B. Garrett, J. Lu, K. Amine, C. Hadad, W. Chen, A. Asthagiri, Y. Wu, Dimeric $[Mo_2S_{12}]^{2-}$ Cluster: A Molecular Analogue of MoS_2 Edges for Superior Hydrogen-Evolution Electrocatalysis, Angew. Chem. Int. Ed. 54 (2015) 15181–15185.

[40] J. McAllister, N. A. G. Bandeira, J. C. McGlynn, A. Y. Ganin, Y.-F. Song, C. Bo, H. N. Miras, Tuning and mechanistic insights of metal chalcogenide molecular catalysts for the hydrogen evolution reaction, Nat. commun. 10, 370, (2019) 1-10.

[41] Y. Li, A. Chernikov, X. Zhang, A. Rigosi, H. M. Hill, A. M. van der Zande, D. A. Chenet, E.-M. Shih, J. Hone, T. F. Heinz, Measurement of the optical dielectric function of transition metal dichalcogenide monolayers: MoS_2, $MoSe_2$, WS_2 and WSe_2, Phys. Rev. B 90 (2014) 205422.

[42] J. Kibsgaard, T. F. Jaramillo, F. Besenbacher, Building an Appropriate Active Site Motif Into a Hydrogen Evolution Catalyst With Thiomolybdate $[Mo_3S_{13}]^{2-}$ Clusters, Nat. Chem. 6 (*2014)* 248–253.

[43] C. G. Morales-Guio, X. Hu, Amorphous Molybdenum Sulfides as Hydrogen Evolution Catalysts, *Acc.* Chem. Res. 47 (2014) 2671−2681.

[44] P. D. Tran, T. V. Tran, M. Orio, S. Torelli, Q. D. Truong, K. Nayuki, Y. Sasaki, S. Y. Chiam, R. Yi, I. Honma, J. Barber, V. Artero, Coordination Polymer Structure and Revisited Hydrogen Evolution Catalytic Mechanism for Amorphous Molybdenum Sulfide, Nat. Mater. 15 (2016) 640–647.

[45] A. Arora, M. Koperski, K. Nogajewski, J. Marcus, Excitonic resonances in thin films of WSe_2: from monolayer to bulk material, Nanoscale **7** (2015) 10421-10429.

[46] Y. Li, J. Shi, H. Chen, R. Wang, Y. Mi, C. Zhang, W. Du, S. Zhang, Z. Liu, Q. Zhang, X. Qiu, H. Xu, W. Liu, Y. Liu, X. Liu, The Auger process in multilayer WSe_2 crystals, Nanoscale 10 (2018) 17585.

[47] M. Zhong, T. Hisatomi, Y. Kuang, J. Zhao, M. Liu, A. Iwase, Q. Jia, H. Nishiyama, T. Minegishi, M. Nakabayashi, N. Shibata, R. Niishiro, C. Katayama, H. Shibano, M. Katayama, A. Kudo, T. Yamada, K. Domen, Surface Modification of CoOx Loaded $BiVO_4$ Photoanodes with Ultrathin p-Type NiO Layers for Improved Solar Water Oxidation, J. Am. Chem. Soc. 137 (2015) 5053−5060.

[48] E.A. Ponomarev, L. M. Peter, A Generalized Theory of Intensity Modulated Photocurrent Spectroscopy (IMPS), J. Electroanal. Chem. 396 (1995) 219-225.

[49] S. Zhang, C. -G. Wang, M. -Y. Li, D. Huang, L. -J. Li, W. Ji, S. Wu, Defect Structure of Localized Excitons in a WSe_2 Monolayer, Phys. Rev. Lett. 119 (2017) 046101 1–6.

[50] Y. Guo, D. Liu, J. Robertson, Chalcogen vacancies in monolayer transition metal dichalcogenides and Fermi level pinning at contacts, Appl. Phys. Lett. 106 (2015) 173106.

[51] J. K. Nørskov, T. Bligaard, A. Logadottir, J. R. Kitchin, J. G. Chen, S. Pandelov, U. Stimming, Trends in the Exchange Current for Hydrogen Evolution, J. Electrochem. Soc. 152, 3 (2005) J 23–6.

[52] W. Kautek, Electronic mobility anisotropy of layered semiconductors: transversal photoconductivity measurements at n-$MoSe_2$, J. Phys. C: Solid State Phys. 15 **(**1982) L519.